Monthly Notices of the ROYAL ASTRONOMICAL SOCIETY

MNRAS **509,** 1147–1159 (2022) https://doi.org/10.1093/mnras/stab3072
Advance Access publication 2021 October 25

Bolometric luminosity estimators using infrared hydrogen lines for dust obscured active galactic nuclei

Dohyeong Kim [1,2]★ Daye Lee [3] and Myungshin Im [2,4]★

[1] *Department of Earth Sciences, Pusan National University, Busan 46241, Republic of Korea*
[2] *Astronomy Program, Department of Physics and Astronomy, Seoul National University, Seoul 08826, Republic of Korea*
[3] *Department of Astronomy, Yonsei University, 50 Yonsei-ro, Seodaemun-gu, Seoul 03722, Republic of Korea*
[4] *SNU Astronomy Research Center (SNU ARC), Astronomy Program, Department of Physics and Astronomy, Seoul National University, Seoul 08826, Republic of Korea*

Accepted 2021 October 19. Received 2021 October 15; in original form 2021 August 26

ABSTRACT

Bolometric luminosity is an important quantity that tells us the radiative energy output of an active galactic nucleus (AGN). A common way to estimate bolometric luminosity is to use ultraviolet (UV) or optical luminosities as its proxies, but the UV- or optical-based-bolometric luminosity estimators can be easily affected by dust extinction. In this study, we present new methods for estimating bolometric luminosities using infrared (IR) hydrogen Paschen and Brackett line luminosities to alleviate the dust extinction effects. We show that there exist tight correlations between the bolometric luminosities and the IR hydrogen line luminosities, and present the IR hydrogen line-based-bolometric luminosity estimators. As an example, we apply the relation to dust obscured red AGNs, confirming previous results that red AGNs have higher Eddington rations than unobscured AGNs. The new bolometric luminosity estimator will be useful for studying obscured AGNs (e.g. red AGNs, Compton thick AGNs, and Type 2 AGNs), during the coming era of sensitive near-infrared (NIR) and mid-infrared (MIR) missions, such as the *James Webb Space Telescope*.

Key words: galaxies: active – quasars: emission lines – quasars: general – quasars: supermassive black holes – infrared: galaxies.

1 INTRODUCTION

Active galactic nuclei (AGNs) refer to the active phase of supermassive black holes (SMBHs) located in the centres of spheroidal galaxies, generating powerful emission fuelled by gas accretion on to the SMBHs. Eddington ratio ($\lambda_{\rm Edd}$: $L_{\rm bol}/L_{\rm Edd}$, where $L_{\rm bol}$ and $L_{\rm Edd}$ are the bolometric and Eddington luminosities, respectively) is a fundamental quantity signifying the AGN activities to understand the evolution of AGNs. The value of $\lambda_{\rm Edd} = 1$ signifies that the accretion is occurring at a maximal rate, while $\lambda_{\rm Edd} = 0$ means no accretion. To determine $\lambda_{\rm Edd}$, two important physical quantities should be measured, $L_{\rm bol}$ and the mass of SMBH.

The $L_{\rm bol}$ value gives the rate of the total radiative energy from an AGN. It has been shown that there are empirical correlations between $L_{\rm bol}$ and X-ray luminosities (e.g. Brightman et al. 2017) or continuum luminosities in UV and optical at 1450 Å, 3000 Å, and 5100 Å (e.g. Runnoe, Brotherton & Shang 2012). Because of their relative ease of measurements, the UV or optical continuum luminosities have been frequently used to estimate $L_{\rm bol}$ values.

In its simplest form, a linear correlation between the UV/optical luminosities and $L_{\rm bol}$ is a common choice when converting X-ray/UV/optical luminosities to $L_{\rm bol}$, although a number of works suggest that a non-linear relation better represents the correlation. In the conversion of UV/optical luminosities to $L_{\rm bol}$, a bolometric correction factor is multiplied to UV/optical luminosities to get $L_{\rm bol}$, a constant value for a conversion using a linear correlation, or luminosity-dependent value with a non-linear correlation. The bolometric corrections are typically about 10 for converting 5100 Å luminosity (hereafter, L5100) to $L_{\rm bol}$ (e.g. Kaspi et al. 2000; Richards et al. 2006), and about 3 to 5 for converting 1450 Å luminosity (hereafter, L1450) to $L_{\rm bol}$ (e.g. Elvis et al. 1994; Runnoe et al. 2012).

However, the application of the empirical relations is problematic for a new population of AGN called red AGNs. Red AGNs have very red colours (e.g. $R - K > 4$ and $J - K > 1.3$ mag; Glikman et al. 2007; Urrutia et al. 2009), and they are considered to be the intermediate population between highly obscured AGNs, often seen as ultraluminous infrared galaxies (ULIRGs; Sanders et al. 1988) and normal unobscured AGNs when major merger between gas-rich galaxies occurs (Di Matteo, Springel & Hernquist 2005). Blowing out gas and dust, previously buried AGN activity becomes visible, but just before that to happen, red AGNs are expected to show high accretion rates, and reddened spectrum because of still remaining gas and dust. This scenario is supported by several observational studies that red AGNs have (i) merging features in their host galaxies (Urrutia, Lacy & Becker 2008; Glikman et al. 2015); (ii) dusty red colours (Kim & Im 2018); (iii) high BH accretion rates (Kim et al. 2015a, 2018); (iv) enhanced star formation activities (Georgakakis et al. 2009); and (v) merging SMBH system (Kim et al. 2020).

The dust extinction of red AGNs ($A_V \sim 1$–5) is moderate compared to type 2 AGNs ($A_V \sim 5$–100) that show only narrow emission lines due to its surrounding torus (Antonucci 1993). For the dust

★ E-mail: dh.dr2kim@gmail.com (DK); m_im@snu.ac.kr (MI)

obscuration resulting in colour excess of $E(B-V)=2$, it would lead to substantial decreases in L5100 and L1450 by a factor of 500 and 5×10^6, respectively. In comparison, NIR and MIR luminosities suffer much less dust extinction, with a luminosity decreasing only by factor of 1.31, 1.62, 2.16, and 3.97 for each Brα (4.05 μm), Brβ (2.63 μm), Pα (1.87 μm), and Pβ (1.28 μm) lines, respectively (Kim, Im & Kim 2010; Kim et al. 2015b). The other studies reported that NIR regime is ten times less obscured compared with optical regime (e.g. Veilleux, Kim & Sanders 2002). In this respect, NIR and MIR emission lines have a clear merit for studying obscured AGN population.

Type 1 AGNs, which show broad emission lines in their spectra, take up more than 50 per cent of red AGNs selected in the radio, NIR, and optical surveys (e.g. Glikman et al. 2007; Urrutia et al. 2009). Among them, however, the $\lambda_{\rm Edd}$ values of only <100 dusty red AGNs have been measured (Urrutia et al. 2012; Kim et al. 2015a; Kim & Im 2018; Kim et al. 2018) due to their dust extinction. Meanwhile, the correlation between Brα, Brβ, Pα, Pβ, and Hα, Hβ lines in flux and full-width at half-maximum (FWHM) of unobscured type 1 AGNs implies that these lines are from the same origin; the ionized gas in the BLR (Kim et al. 2010, 2015b). These studies imply that the broad hydrogen Paschen and Brackett lines, which are the main subject of this work, are likely observed frequently and can replace the role of hydrogen Balmer lines. Since the BLR is ionized by radiation from accretion disc, strong emission lines are induced for luminous AGNs. The objective of this paper is to examine correlations between IR emission lines and the bolometric luminosity of AGNs and establish a bolometric correction which can be used for future works studying properties of dust obscured AGNs, such as red AGNs and type 2 AGNs.

In this work, we find tight correlations between the bolometric luminosities with the IR hydrogen Paschen and Brackett line luminosities. We expect bolometric corrections using the IR hydrogen lines will be alternative bolometric luminosity indicators relatively immune from the dust extinction effects. Throughout this work, we adopt a standard ΛCDM model of $H_0=70\,{\rm km\,s^{-1}\,Mpc^{-1}}$, $\Omega_m=0.3$, and $\Omega_\Lambda=0.7$ that is supported by past observational studies (e.g. Im, Griffiths & Ratnatunga 1997; Planck Collaboration VIII 2011; Planck Collaboration XIII 2016).

2 SAMPLE AND DATA

We present the sample with which we derive functions to convert IR line luminosities to $L_{\rm bol}$ values. The sample is composed of 48 unobscured type 1 AGNs at low redshifts ($0.001<z<0.378$) for which Paschen/Brackett line luminosities and $L_{\rm bol}$ values are available in the literature. This sample spans a wide range of $L_{\rm bol}$ ($10^{41.4}$ to $10^{47.3}\,{\rm erg\,s^{-1}}$). Among them, BH masses of 42 objects are available in three previous papers (Peterson et al. 2004; Vestergaard & Peterson 2006; Kim et al. 2010), and we use the BH masses after applying a recent virial coefficient of $\log f=0.05$ (Woo et al. 2015) in this study. For the 42 objects, the BH masses range from $10^{6.28}$ to $10^{9.44}\,M_\odot$ with $-2.94<\log(\lambda_{\rm Edd})<0.590$. For the other 6 objects, they are used for deriving the bolometric luminosity indicators without the BH mass and $\lambda_{\rm Edd}$ informations. Figs 1 and 2 show the $L_{\rm bol}$, $M_{\rm BH}$, and $\lambda_{\rm Edd}$ distributions, as well as $L_{\rm bol}$ versus $M_{\rm BH}$ of the sample. We describe below, where each quantity is taken and how the values were derived in the literature.

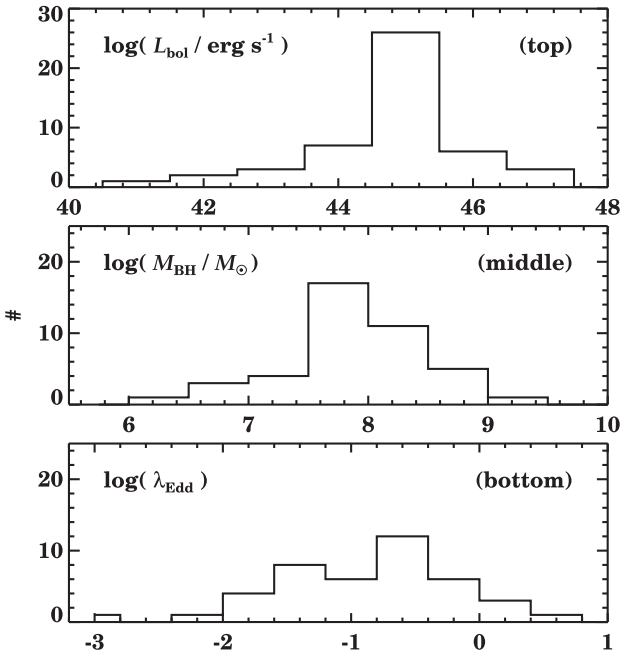

Figure 1. Distributions of $L_{\rm bol}$, $M_{\rm BH}$, and $\lambda_{\rm Edd}$ of our sample AGNs. These distributions show that our sample covers wide ranges of $L_{\rm bol}$ ($10^{41.4}$–$10^{47.3}\,{\rm erg\,s^{-1}}$), $M_{\rm BH}$ ($10^{6.28}$–$10^{9.44}\,M_\odot$), and $\log(\lambda_{\rm Edd})$ (−2.94–0.59).

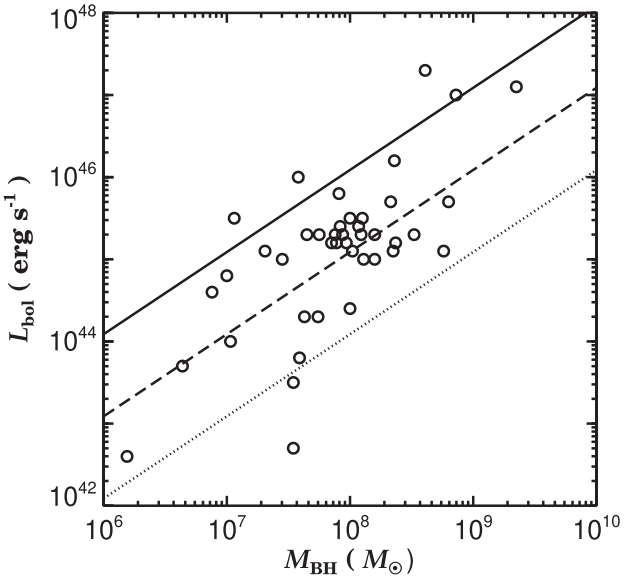

Figure 2. Comparison between $L_{\rm bol}$ and $M_{\rm BH}$ values for our sample. The solid, dashed, and dotted lines mean $\lambda_{\rm Edd}$ of 1, 0.1, and 0.01, respectively.

2.1 Paschen and Brackett line fluxes

Paschen line fluxes are taken from three papers (Riffel, Rodríguez-Ardila & Pastoriza 2006; Kim et al. 2010; Lamperti et al. 2017) as described below.

Kim et al. (2010, hereafter, K10) used 37 type 1 AGNs for establishing Paschen line-based BH mass estimators. Their data come from two main sources, 23 from Landt et al. (2008, hereafter, L08) and 26 from Glikman et al. (2006, hereafter, G06). The G06 sample studied by K10 is made of type 1 AGNs with $K<14.5$ mag, $z<0.5$, and $M_i<-23$ mag, and K10 derived NIR fluxes and line widths from

the G06 spectra, applying a single Gaussian fitting to the lines. On the other hand, they took the broad emission line fluxes from L08 who studied NIR spectra of 23 well-known type 1 AGNs. K10 excluded four sources, Mrk 590, NGC 5548, Ark 564, and NGC 7469, from L08 AGNs in their $M_{\rm BH}$ estimator derivation because of uncertain line width values. These four sources, however, have reliable line fluxes, so we added them in our analysis. After matching with a list of sources with $L_{\rm bol}$, the number of adopted K10 AGNs is 34.

Riffel et al. (2006, hereafter, R06) provide fluxes of various emission lines in 0.8–2.4 μm as well as continuum fluxes for well studied 47 AGNs. The 47 AGNs are at $z < 0.55$, and composed of 7 quasars, 25 type 1 AGNs, and 15 type 2 AGNs. In this work, we use 13 type 1 AGNs, including 4 quasars, of the R06 AGNs for which $L_{\rm bol}$ values are available in the literature.

Lamperti et al. (2017, hereafter, L17) analysed NIR spectra of 102 nearby ($z < 0.075$) AGNs selected from the Swift/BAT 70-months catalogue where their NIR spectra come from their own observations or from literatures (L08). They provide measurements of FWHMs and fluxes of emission lines in NIR. Among them, we use 21 type 1 AGNs from their study that have corresponding $L_{\rm bol}$ values in the literature.

Note that the line fluxes from these studies (R06, L08, K10, L17) are derived with a single Gaussian fitting to the broad line component. K10 compared the flux values from a single Gaussian fitting ($F_{\rm single}$) and a multiple Gaussian fitting ($F_{\rm multi}$) to broad lines, and found that $F_{\rm multi}/F_{\rm single} = 1.08$. For the literature values derived from a single Gaussian fitting, we apply this correction factor.

In the end, there are 48 AGNs with Paschen line information and available bolometric luminosities. These objects are listed in Table 1. For 15 of these objects, the Paschen line fluxes are available in more than one reference. The multiple Paschen line flux measurements of the samples are given in Table 2, and Fig. 3 compares the Paschen line fluxes from the literature, by presenting the ratio of the literature values to the average of the literature values. The average rms dispersion of the ratios are found to be about 0.07 dex that corresponds to ∼20 per cent uncertainty. To provide a realistic error on the flux measurements, this rms dispersion is added in quadrature to the measurement uncertainties presented in the literature. For several AGNs, the Paschen line fluxes are different by more than a factor of 2. These objects are Mrk 509, NGC 4151, NGC 3227, and NGC 5548. Although L17 analysed the same spectra from L08 whose values were adopted in K10, the values are significantly different for these cases. L17 suggested that this discrepancy could arise from the different fitting method. L08 fit the broad lines after subtracting the narrow lines, but the broad and narrow lines were fitted simultaneously in L17. For these four cases, we adopt the rms dispersion of the values from different literatures as the line flux error.

For obtaining the Brackett line luminosities, we use the Brackett line measurements measured in Kim et al. (2015b). Since the Brackett lines in MIR are difficult to observe from the ground due to the atmospheric absorption and strong thermal sky background, the *AKARI* 2.5–5.0 μm spectroscopic study of Kim et al. (2015b) solely provide Br β and Br α line fluxes. Since Kim et al. (2015b) measured the Brackett line fluxes using a single Gaussian fitting without removing the narrow component, we apply a fitting method correction factor of 1.06 (Kim et al. 2010) to the Brackett line fluxes, similar to the Paschen line analysis. Note that Kim et al. (2010) compared the flux values from a single Gaussian fitting without removing narrow component ($F_{\rm single,+narrow}$) and $F_{\rm multi}$, and found that $F_{\rm multi}/F_{\rm single,+narrow}$ is 1.06.

2.2 Bolometric luminosities

Measuring the bolometric luminosity accurately is a difficult task. It takes a significant amount of efforts to conduct full wavelength observation. Furthermore, the variable nature of AGN emissions makes the task more complicated, since it requires simultaneous observations in all wavelength range. Also, the intergalactic hydrogen atoms absorb extreme UV part of spectrum, which is observed as Lyman forest and makes it more difficult to trace the shape of SED. Interpolation of the observed SED and exclusion of the host galaxy light are other factors to consider when obtaining bolometric luminosity. The main concerns can be summarized as follows. (1) The coverage of observational data used to construct the SED; (2) the wavelength range for integrating specific luminosities; (3) the interpolation method or assumed model to fit the lack of observation; and (4) the correction for host galaxy contamination.

Deciding integration wavelength limits for estimating the bolometric luminosity is a tricky problem, and there are diverse choices made in the literature. Marconi et al. (2004) suggested that IR flux should not be counted because the accretion disc photons are reprocessed into IR emission by dusty torus surrounding the disc and including such as IR emission component would effectively be a double-counting.

A similar controversy arises in the hard X-ray (>2 keV). Hard X-ray is known to be produced from inverse-Compton upscattering of disc photons by electrons in hot corona. Whether these photons are reprocessed depends on the geometry of corona, such as whether corona is spherical shape, or patchy skin attached to the accretion disc (Sobolewska, Siemiginowska & Życki 2004a,b). Most of the previous works counts photons from 1 μm, excluding IR emission, and to 10 keV or 100 keV. However, in contrast to IR emission whose energy budget is comparable to optical/UV luminosity, X-ray luminosity takes up a small portion of the AGN total luminosity (e.g. Richards et al. 2006). Therefore, we do not distinguish bolometric luminosities obtained over different integration limits of 1 μm–10 keV and 1 μm–100 keV. Vasudevan & Fabian (2007, hereafter, VF07) set an integration limit as 0.001–250 keV, which may be considered too deviating from others. Note that 0.001 keV corresponds to ∼1 μm. We checked the 14–195 keV band luminosity from Baumgartner et al. (2013) for these sources, and we find that the 14–195 keV band luminosity takes a very small portion of the $L_{\rm bol}$ values (∼18 per cent). Therefore, we even consider the VF07 values as provided.

VF07, Vasudevan & Fabian (2009, hereafter, VF09), and Vasudevan et al. (2009, hereafter, V09) adopted a broken power-law accretion disc model to fit the observed AGN SED over a range of X-ray to UV/optical. Accretion disc model essentially characterizes blackbody spectrum and Big Blue Bump (BBB) in the UV. The broken power-law model adopted to fit the X-ray part prevents extrapolation of power law over UV-optical region. The works of VF09 and V09 employed simultaneous observation which was effective in controlling SED shape as they reported. However, their SED fitting model is prone to variability as small change of optical-UV flux can be extrapolated into large change in bolometric luminosity when summed up. The authors discussed 20 percent of flux variation in *UV* band would contribute to change accretion disc luminosity ($L_{0.001-0.1\,\rm keV}$) up to a factor of two. Multiple observations of the same objects give considerably different bolometric luminosity for some cases, from 0.1 dex to 0.5 dex, presumably because of variability.

Krawczyk et al. (2013, hereafter, K13) constructed the SED using broad-band data from MIR to far-UV (FUV) for the SDSS DR7

Table 1. Sample.

Name	Redshift (z)	R.A. (J2000.0)	Dec. (J2000.0)	$M_{\rm BH}$ ($M_\odot$)
Mrk 590	0.026	02:14:33.56	−00:46:00.2	$10^{7.59\pm0.06}$
3C 120	0.033	04:33:11.10	+05:21:15.6	$10^{7.65\pm0.17}$
Ark 120	0.032	05:16:11.41	−00:08:59.2	$10^{8.09\pm0.05}$
Mrk 79	0.022	07:42:32.82	+49:48:34.8	$10^{7.63\pm0.11}$
Mrk 110	0.035	09:25:12.85	+52:17:10.4	$10^{7.31\pm0.09}$
NGC 3227	0.004	10:23:30.57	+19:51:54.3	$10^{7.54\pm0.18}$
NGC 3516	0.009	11:06:47.46	+72:34:07.2	$10^{7.54\pm0.13}$
NGC 4051	0.002	12:03:09.61	+44:31:52.7	$10^{6.19\pm0.15}$
NGC 4151	0.003	12:10:32.58	+39:24:21.1	$10^{7.03\pm0.13}$
NGC 4593	0.009	12:39:39.44	−05:20:39.0	$10^{6.64\pm0.38}$
Mrk 279	0.030	13:53:03.44	+69:18:29.4	$10^{7.45\pm0.10}$
NGC 5548	0.017	14:17:59.54	+25:08:12.6	$10^{7.74\pm0.02}$
3C 390.3	0.056	18:42:08.99	+79:46:17.1	$10^{8.37\pm0.09}$
NGC 7469	0.016	23:03:15.67	+08:52:25.3	$10^{7.00\pm0.05}$
Mrk 766	0.013	12:18:26.52	+29:48:46.5	–
IRAS 05589+2828	0.033	06:02:10:32	+28:28:04.8	–
Mrk 290	0.030	15:35:52.40	+57:54:09.5	$10^{8.00\pm0.04}$
NGC 4395	0.001	12:25:48.86	+33:32:48.7	–
NGC 6814	0.005	19:42:40.59	−10:19:25.1	–
Ark 564	0.025	22:42:39.34	+29:43:31.3	–
Mrk 335	0.026	00:06:19.54	+20:12:10.6	$10^{7.06\pm0.10}$
Mrk 876	0.129	16:13:57.18	+65:43:10.0	$10^{8.36\pm0.17}$
Mrk 509	0.034	20:44:09.75	−10:43:24.7	$10^{8.07\pm0.03}$
3C 273	0.158	12:29:06.70	+02:03:08.6	$10^{8.86\pm0.08}$
PG 0844+349	0.064	08:47:42.45	+34:45:04.5	$10^{7.88\pm0.15}$
PG 1415+451	0.114	14:17:00.82	+44:56:06.3	$10^{7.92\pm0.09}$
Mrk 478	0.078	14:42:07.47	+35:26:22.9	–
PG 1519+226	0.137	15:21:14.26	+22:27:47.8	$10^{7.85\pm0.09}$
PG 1612+261	0.131	16:14:13.20	+26:04:16.2	$10^{7.97\pm0.09}$
PG 1448+273	0.065	14:51:08.76	+27:09:27.0	$10^{6.88\pm0.09}$
SDSS J000943.1−090839.2	0.210	00:09:43.14	−09:08:39.2	$10^{8.35\pm0.04}$
SDSS J005812.8+160201.3	0.211	00:58:12.85	+16:02:01.3	$10^{8.20\pm0.04}$
SDSS J010226.3−003904.6	0.295	01:02:26.31	−00:39:04.6	$10^{7.58\pm0.04}$
SDSS J011110.0−101631.8	0.179	01:11:10.04	−10:16:31.8	$10^{8.11\pm0.04}$
SDSS J015530.0−085704.0	0.165	01:55:30.02	−08:57:04.0	$10^{8.76\pm0.04}$
SDSS J015910.0+010514.5	0.217	01:59:10.05	+01:05:14.5	$10^{7.89\pm0.04}$
SDSS J015950.2+002340.8	0.163	01:59:50.24	+00:23:40.8	$10^{8.00\pm0.04}$
SDSS J021707.8−084743.4	0.292	02:17:07.87	−08:47:43.4	$10^{7.75\pm0.04}$
SDSS J024250.8−075914.2	0.378	02:42:50.85	−07:59:14.2	$10^{7.91\pm0.04}$
SDSS J031209.2−081013.8	0.265	03:12:09.20	−08:10:13.8	$10^{8.20\pm0.04}$
SDSS J032213.8+005513.4	0.185	03:22:13.89	+00:55:13.4	$10^{7.94\pm0.04}$
SDSS J150610.5+021649.9	0.135	15:06:10.50	+02:16:49.9	$10^{8.02\pm0.04}$
SDSS J172711.8+632241.8	0.218	17:27:11.81	+63:22:41.8	$10^{8.52\pm0.04}$
SDSS J211843.2−063618.0	0.328	21:18:43.24	−06:36:18.0	$10^{8.33\pm0.04}$
SDSS J234932.7−003645.8	0.279	23:49:32.77	−00:36:45.8	$10^{8.10\pm0.04}$
SDSS J235156.1−010913.3	0.174	23:51:56.12	−01:09:13.3	$10^{8.80\pm0.04}$
PDS 456	0.184	17:28:19.79	−14:15:55.9	$10^{8.61\pm0.04}$
H 1821+643	0.297	18:21:57.24	+64:20:36.2	$10^{9.35\pm0.04}$

quasars. Lack of X-ray data was replaced using a $L_{\rm UV}$–$L_{\rm X}$ relation (Steffen et al. 2006), which enables estimating 2 keV luminosity from 2500 Å luminosity. The unobserved extreme-UV (EUV) range was interpolated by a simple power law connecting UV and X-ray data points. Host galaxy contamination was removed by modelling host galaxy contribution from previous works. We compared bolometric luminosities in Krawczyk et al. (2013) with those of Richards et al. (2006) for 250 overlapped sample, and the rms difference of bolometric luminosities was 0.07. Note that Richards et al. (2006) constructed their SEDs using similar methods, such as correcting host galaxy contamination and using the $L_{\rm UV}$–$L_{\rm X}$ relation due to the lack of X-ray data. Hence, the measurements of Krawczyk et al. (2013) are quite reasonable despite of the absence of X-ray data.

Shang et al. (2011, hereafter, S11) is one of the most well-known studies on quasar SED. They covered a full wavelength range from radio to X-ray and constructed mean quasar energy distribution to understand the spectral properties of quasars. S11 improved the work of Elvis et al. (1994) by updating observational data with newer observations and adding MIR data. Runnoe et al. (2012) subsequently calculated bolometric luminosity by integrating the SED from 1 μm to 8 keV for 63 sources out of 85 sources in S11 with sufficient wavelength coverage. S11 removed the host galaxy contribution

Table 2. Multiple measurements of Paschen line fluxes from different references.

Name	$f_{P\beta}$ L17	$f_{P\beta}$ R06	$f_{P\beta}$ K10	$f_{P\alpha}$ L17	$f_{P\alpha}$ R06	$f_{P\alpha}$ K10
Mrk 335	126 ± 1	–	167 ± 17	137 ± 2	–	140 ± 14
Mrk 590	–	–	14.6 ± 1.5	32.5 ± 1.5	–	28.2 ± 2.8
Ark 120	536 ± 1	–	589 ± 59	732 ± 3	–	696 ± 70
Mrk 79	174 ± 1	–	186 ± 19	314 ± 3	–	258 ± 26
Mrk 110	140 ± 1	–	150 ± 15	189 ± 1	–	199 ± 20
NGC 3227	308 ± 7	182 ± 11	348 ± 35	–	229 ± 5	–
NGC 4051	65.9 ± 1.6	71.9 ± 1.8	–	<173	120 ± 5	–
NGC 4151	822 ± 4	769 ± 9	1210 ± 120	1370 ± 40	628 ± 13	–
NGC 4593	269 ± 1	–	287 ± 29	239 ± 2	–	–
Mrk 279	67.0 ± 0.4	60.3 ± 2.7	–	–	18.8 ± 0.5	–
NGC 5548	110 ± 1	53.2 ± 3.1	177 ± 18	–	85.2	164 ± 16
Ark 564	–	63.8 ± 1.7	71.5 ± 7.2	–	54.8 ± 3	110 ± 11
Mrk 509	473 ± 1	1970 ± 80	520 ± 52	663 ± 1	4020 ± 30	660 ± 66
NGC 7469	130 ± 2	165 ± 8	172 ± 17	114 ± 4	223 ± 12	173 ± 17
PG 0844+349	126 ± 1	–	106 ± 11	120 ± 0	–	121 ± 12

Note. Multiple measurements of Paschen line flux from several references. The flux unit is 10^{-15} erg s^{-1} cm^{-2}. All the Paschen line fluxes listed in here were taken from SpeX on NASA IRTF.

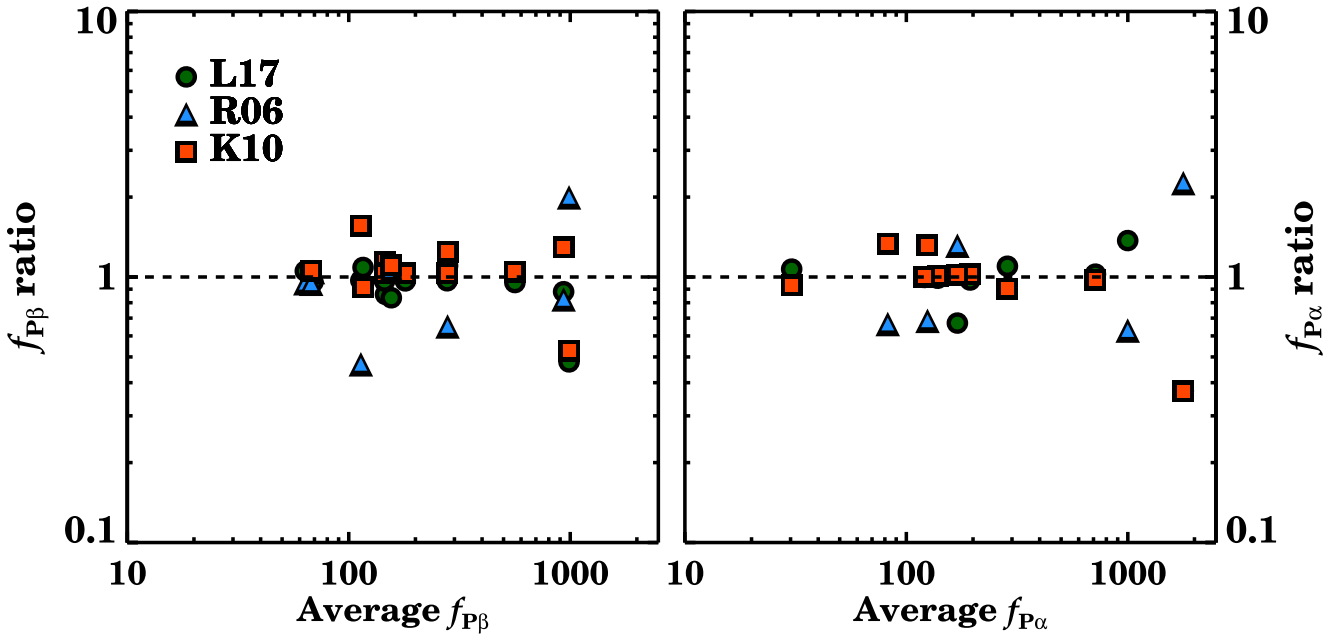

Figure 3. The ratio of the Paschen line fluxes from the literature, normalized to the average of the literature values. The Paschen line fluxes are in units of 10^{-15} erg s^{-1} cm^{-2}.

in NIR by fitting galaxy templates and used a simple power-law interpolation to connect the gap between UV and X-ray.

To supplement high luminosity AGNs at $L_{bol} \sim 10^{47}$ erg s^{-1}, we added PDS 456 and H 1821+643 to our sample. The bolometric luminosity of PDS 456 was approximately estimated as 2×10^{47} erg s^{-1} in Reeves et al. (2009). The bolometric luminosity estimated using the 5100 Å monochromatic luminosity gives 1.8×10^{47} erg s^{-1}, which is consistent with the Reeves et al. (2009) value. Ruiz et al. (2010) presented the bolometric luminosity of H 1821+643 (IRAS 18216+6418), which is classified as a hyperluminous infrared galaxy ($L_{IR} > 10^{13}\ L_{\odot}$). By subtracting IR luminosity ($L_{IR} = 10^{47.1}$ erg s^{-1}) from total luminosity ($L_{bol} = 10^{47.4}$ erg s^{-1}), we obtain the luminosity from 1 μm to 10 keV of $L_{bol} = 10^{47.1}$ erg s^{-1} if we ignore the radio contribution. The details of the L_{bol} references are summarized in Table 3.

Nearly half of our sample in the cross-match list with Paschen lines have multiple L_{bol} measurements from several references. It is hard to figure out which result gives the most accurate estimation. However, S11 used the most extensive multiwavelength data to construct SED, and we prioritize values from S11. For the rest of sample, we choose the values from VF09 for the consistency of the measurement method for the rest of the overlapping sample. Table 4 shows the different estimates of bolometric luminosity from several references for those having duplicated measurements, and Fig. 4 shows a comparison of the bolometric luminosity measurements from different references. We calculated the rms scatter of multiple values of each sample.

Table 3. L_{bol} references and definitions.

Reference	Data	Integration limits
VF07	X-ray, UV	0.001–250 keV
VF09	X-ray, UV, optical	0.001–100 keV
V09	X-ray, UV, optical	0.001–100 keV
S11 (measured in Runnoe et al. 2012)	X-ray, UV, optical, NIR, MIR, FIR, radio	1 μm–8 keV
K13	UV, optical, NIR, MIR	1 μm–10 keV

Table 4. Multiple measurements of bolometric luminosity from several references.

	L_{bol} (erg s^{-1})					
Name	VF09	V09	VF07	S11	K13	rms scatter
3C 120	$10^{45.3}$	$10^{44.9}$	–	–	–	0.20
3C 390.3	$10^{45.2}$	$10^{45.3}$	–	–	–	0.05
Ark 120	$10^{45.3}$	$10^{45.1}$	$10^{45.0}$	–	–	0.12
Mrk 79	$10^{44.3}$	–	$10^{44.3}$	–	–	0.00
Mrk 279	$10^{45.0}$	$10^{44.4}$	$10^{45.0}$	–	–	0.28
Mrk 335	$10^{45.3}$	–	$10^{45.2}$	–	–	0.05
Mrk 509	$10^{45.2}$	$10^{44.9}$	$10^{45.1}$	$10^{45.4}$	–	0.17
Mrk 590	$10^{43.8}$	$10^{43.6}$	–	–	–	0.10
NGC 3227	$10^{42.9}$	–	$10^{43.1}$	–	–	0.29
NGC 3783	$10^{44.2}$	–	$10^{44.3}$	–	–	0.08
NGC 4151	$10^{44.0}$	–	–	–	–	–
NGC 4593	$10^{43.7}$	$10^{43.6}$	$10^{43.7}$	–	–	0.04
NGC 5548	$10^{44.3}$	$10^{44.1}$	–	–	–	0.10
NGC 7469	$10^{44.8}$	$10^{44.3}$	$10^{44.5}$	–	–	0.21
PG 0052+251	$10^{45.8}$	–	$10^{45.9}$	$10^{45.9}$	–	0.06
PG 0844+349	$10^{45.4}$	–	$10^{45.2}$	$10^{45.3}$	–	0.08
3C 273	$10^{47.1}$	–	$10^{47.1}$	$10^{47.0}$	–	0.05
PG 1411+442	$10^{45.4}$	–	–	$10^{45.3}$	–	0.04
PG 1415+451	–	–	$10^{45.1}$	$10^{45.4}$	$10^{44.9}$	0.18
Mrk 478	–	–	$10^{45.4}$	$10^{45.6}$	–	0.12

Note. Multiple measurements of bolometric luminosity from several references. The L_{bol} measurements are presented in logarithmic scale, and the L_{bol} unit is erg s^{-1}.

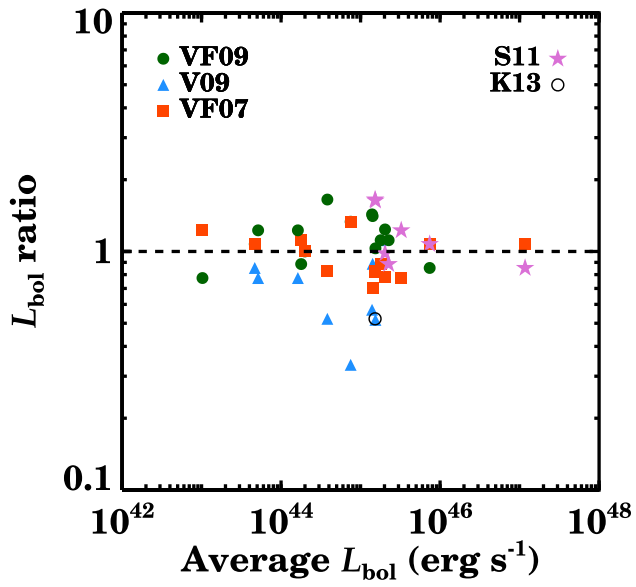

Figure 4. The ratios of bolometric luminosities adopted from several references, normalized to the average of the literature values.

There was no particular tendency between the rms and average of bolometric luminosities, and the average of scatter was 0.14 dex which means ∼38 per cent uncertainty. We set the rms scatter of each sample as the uncertainty of the bolometric luminosity, and apply the average rms scatter as uncertainties for that do not have multiple measurements.

3 BOLOMETRIC CORRECTION IN IR EMISSION LINE

After cross-matching different samples as above, we construct a list of Paschen-bolometric luminosity pairs as well as Brackett-bolometric luminosity pairs. The list is presented in Table 5 for the Paschen lines and Table 6 for the Brackett lines with remarks on which reference was chosen for a given pair of the Paschen/Brackett line and the bolometric luminosity.

To build the relation between the Paschen line luminosity and the bolometric luminosity, we first assumed a non-linear relationship as,

$$\log\left(\frac{L_{bol}}{10^{42}\,\mathrm{erg\,s^{-1}}}\right) = \mathrm{A} + \mathrm{B}\log\left(\frac{L_{Paschen}}{10^{40}\,\mathrm{erg\,s^{-1}}}\right), \quad (1)$$

where we linearly fit the data in log–log plane by setting two free variables; the slope (B) and the Y-intercept (A).

The linear fitting on the log–log plane was performed with an updated version of MPFITEXY (Markwardt 2009; Williams, Bureau & Cappellari 2010) on Interactive Data Language (IDL). The program takes into account of errors on both X and Y variables as well as intrinsic scatter. The intrinsic scatter is iteratively adjusted until it makes the reduced chi-square close to unity. Figs 5 and 6 show the best-fitting results of Paschen and Brackett line versus bolometric luminosity and the values of the slope and Y-intercept are listed in Table 7. We note that the scatter in the correlations are dominated by the intrinsic scatter, with the values ranging from 0.31 dex to 0.38 dex. These values are also listed in Table 7.

Additionally, we derive relations between the IR line luminosities and the bolometric luminosities as expected in the linear relationship. The slope term B in equation (1) is fixed to 1, and the yielded relations are presented in Figs 5 and 6, and Table 7. The results are not significantly different from the non-linear relation results.

4 DISCUSSION

4.1 Dependence of bolometric correction on SMBH activities

The bolometric correction may have a dependence on SMBH activity parameters, such as the bolometric luminosity or λ_{Edd} (e.g. Lusso et al. 2012). Therefore, we test whether the bolometric corrections using the Paschen line luminosities change with the SMBH activities. Lusso et al. (2012) showed that the bolometric corrections using the X-ray luminosities have a tendency to increase at high bolometric luminosities ($L_{bol} > 10^{44}$ erg s^{-1}). We compare the ratios of the bolometric luminosities and the Paschen line luminosities as a

Table 5. Paschen line and bolometric luminosities.

Name	$L_{P\beta}$ (erg s^{-1})	$L_{P\alpha}$ (erg s^{-1})	L_{bol} (erg s^{-1})	log (λ_{Edd})
Mrk 590	$10^{40.37 \pm 0.09}$(a)	$10^{40.65 \pm 0.05}$(a)	$10^{43.8 \pm 0.1}$	–1.89 ± 0.11
3C 120	$10^{41.81 \pm 0.08}$(b)	$10^{41.96 \pm 0.08}$(b)	$10^{45.3 \pm 0.2}$	–0.45 ± 0.22
Ark 120	$10^{42.11 \pm 0.03}$(a)	$10^{42.24 \pm 0.01}$(a)	$10^{45.3 \pm 0.1}$	–0.89 ± 0.10
Mrk 79	$10^{41.29 \pm 0.02}$(a)	$10^{41.54 \pm 0.04}$(a)	$10^{44.3 \pm 0.0}$	–1.43 ± 0.11
Mrk 110	$10^{41.60 \pm 0.02}$(a)	$10^{41.73 \pm 0.02}$(a)	$10^{45.1 \pm 0.1}$	–0.31 ± 0.12
NGC 3227	$10^{39.78 \pm 0.13}$(a)	$10^{39.88 \pm 0.08}$(a)	$10^{42.9 \pm 0.3}$	–2.74 ± 0.27
NGC 3516	$10^{40.56 \pm 0.08}$(b)	$10^{40.24 \pm 0.08}$(b)	$10^{43.5 \pm 0.1}$	–2.14 ± 0.15
NGC 4051	$10^{38.92 \pm 0.02}$(a)	$10^{39.14 \pm 0.08}$(a)	$10^{42.6 \pm 0.1}$	–1.69 ± 0.17
NGC 4151	$10^{40.26 \pm 0.09}$(a)	$10^{40.18 \pm 0.17}$(a)	$10^{44.0 \pm 0.1}$	–1.13 ± 0.15
NGC 4593	$10^{40.68 \pm 0.02}$(a)	$10^{40.63 \pm 0.08}$(a)	$10^{43.7 \pm 0.0}$	–1.04 ± 0.38
Mrk 279	$10^{41.10 \pm 0.03}$(a)	$10^{40.60 \pm 0.08}$(a)	$10^{45.0 \pm 0.3}$	–0.55 ± 0.24
NGC 5548	$10^{41.07 \pm 0.27}$(a)	$10^{41.04 \pm 0.15}$(a)	$10^{44.3 \pm 0.1}$	–1.54 ± 0.09
3C 390.3	$10^{41.35 \pm 0.18}$(b)	$10^{41.81 \pm 0.08}$(b)	$10^{45.2 \pm 0.1}$	–1.27 ± 0.12
NGC 7469	$10^{40.99 \pm 0.06}$(a)	$10^{41.12 \pm 0.15}$(a)	$10^{44.8 \pm 0.2}$	–0.30 ± 0.17
Mrk 766	$10^{40.66 \pm 0.08}$(a)	$10^{40.64 \pm 0.08}$(a)	$10^{44.1 \pm 0.1}$	–
IRAS 05589+2828	–	$10^{42.81 \pm 0.08}$(a)	$10^{44.7 \pm 0.1}$	–
Mrk 290	$10^{41.51 \pm 0.09}$(a)	$10^{41.53 \pm 0.09}$(a)	$10^{44.4 \pm 0.1}$	–1.70 ± 0.10
NGC 4395	$10^{37.97 \pm 0.08}$(b)	$10^{38.13 \pm 0.08}$(b)	$10^{41.4 \pm 0.1}$	–
NGC 6814	$10^{39.99 \pm 0.08}$(a)	–	$10^{42.3 \pm 0.1}$	–
Ark 564	$10^{40.94 \pm 0.08}$(a)	$10^{40.88 \pm 0.09}$(a)	$10^{44.2 \pm 0.1}$	–
Mrk 335	$10^{41.28 \pm 0.06}$(a)	$10^{41.32 \pm 0.01}$(a)	$10^{45.3 \pm 0.1}$	0.14 ± 0.13
Mrk 876	$10^{42.53 \pm 0.09}$(a)	$10^{42.76 \pm 0.09}$(a)	$10^{46.2 \pm 0.2}$	–0.26 ± 0.22
Mrk 509	$10^{42.11 \pm 0.28}$(a)	$10^{42.26 \pm 0.37}$(a)	$10^{45.4 \pm 0.2}$	–0.77 ± 0.17
3C 273	$10^{43.68 \pm 0.09}$(a)	$10^{43.75 \pm 0.09}$(a)	$10^{47.0 \pm 0.1}$	0.04 ± 0.11
PG 0844+349	$10^{42.09 \pm 0.03}$(a)	$10^{42.07 \pm 0.01}$(a)	$10^{45.3 \pm 0.1}$	–0.68 ± 0.17
PG 1415+451	$10^{41.84 \pm 0.08}$(a)	$10^{41.89 \pm 0.08}$(a)	$10^{45.4 \pm 0.2}$	–0.62 ± 0.18
Mrk 478	$10^{42.12 \pm 0.09}$(a)	$10^{41.95 \pm 0.08}$(a)	$10^{45.6 \pm 0.1}$	–
PG 1519+226	$10^{41.84 \pm 0.09}$(a)	$10^{41.98 \pm 0.09}$(a)	$10^{45.2 \pm 0.1}$	–0.75 ± 0.12
PG 1612+261	$10^{42.27 \pm 0.08}$(a)	$10^{42.49 \pm 0.08}$(a)	$10^{45.2 \pm 0.1}$	–0.87 ± 0.12
PG 1448+273	–	$10^{40.42 \pm 0.08}$(a)	$10^{44.6 \pm 0.1}$	–0.38 ± 0.12
SDSS J000943.1−090839.2	$10^{42.03 \pm 0.12}$(a)	$10^{42.03 \pm 0.12}$(a)	$10^{45.1 \pm 0.1}$	–1.35 ± 0.10
SDSS J005812.8+160201.3	$10^{42.35 \pm 0.09}$(a)	$10^{42.46 \pm 0.09}$(a)	$10^{45.0 \pm 0.1}$	–1.30 ± 0.10
SDSS J010226.3−003904.6	$10^{42.83 \pm 0.09}$(a)	$10^{42.90 \pm 0.09}$(a)	$10^{46.0 \pm 0.1}$	0.32 ± 0.10
SDSS J011110.0−101631.8	$10^{42.12 \pm 0.09}$(a)	$10^{42.10 \pm 0.10}$(a)	$10^{45.0 \pm 0.1}$	–1.21 ± 0.10
SDSS J015530.0−085704.0	$10^{42.06 \pm 0.10}$(a)	$10^{42.01 \pm 0.10}$(a)	$10^{45.1 \pm 0.1}$	–1.76 ± 0.10
SDSS J015910.0+010514.5	$10^{42.14 \pm 0.10}$(a)	$10^{42.15 \pm 0.11}$(a)	$10^{45.2 \pm 0.1}$	–0.79 ± 0.10
SDSS J015950.2+002340.8	$10^{42.29 \pm 0.09}$(a)	$10^{42.44 \pm 0.09}$(a)	$10^{45.5 \pm 0.1}$	–0.60 ± 0.10
SDSS J021707.8−084743.4	$10^{41.98 \pm 0.14}$(a)	–	$10^{45.3 \pm 0.1}$	–0.55 ± 0.10
SDSS J024250.8−075914.2	$10^{42.66 \pm 0.10}$(a)	–	$10^{45.8 \pm 0.1}$	–0.21 ± 0.10
SDSS J031209.2−081013.8	$10^{42.39 \pm 0.11}$(a)	–	$10^{45.3 \pm 0.1}$	–1.00 ± 0.10
SDSS J032213.8+005513.4	$10^{42.40 \pm 0.09}$(a)	$10^{42.52 \pm 0.09}$(a)	$10^{45.3 \pm 0.1}$	–0.74 ± 0.10
SDSS J150610.5+021649.9	–	$10^{42.04 \pm 0.09}$(a)	$10^{45.1 \pm 0.1}$	–1.02 ± 0.10
SDSS J172711.8+632241.8	–	$10^{42.20 \pm 0.12}$(a)	$10^{45.3 \pm 0.1}$	–1.32 ± 0.10
SDSS J211843.2−063618.0	$10^{42.37 \pm 0.11}$(a)	–	$10^{45.7 \pm 0.1}$	–0.73 ± 0.10
SDSS J234932.7−003645.8	$10^{42.40 \pm 0.10}$(a)	–	$10^{45.5 \pm 0.1}$	–0.70 ± 0.10
SDSS J235156.1−010913.3	$10^{42.57 \pm 0.09}$(a)	$10^{42.64 \pm 0.09}$(a)	$10^{45.7 \pm 0.1}$	–1.20 ± 0.10
PDS 456	$10^{43.56 \pm 0.09}$(a)	$10^{43.65 \pm 0.09}$(a)	$10^{47.3 \pm 0.1}$	0.59 ± 0.10
H 1821+643	$10^{43.73 \pm 0.09}$(a)	–	$10^{47.1 \pm 0.1}$	–0.35 ± 0.10

Notes. Paschen line and bolometric luminosities of AGNs searched through the cross-match of Paschen line luminosity data and bolometric luminosity measurements done by SED fitting.
[(a)]The Paschen line luminosity was taken from SpeX on NASA IRTF.
[(b)]The Paschen line luminosity was taken from GNIRS on Gemini.

function of the bolometric luminosity, and the comparison is shown in Fig. 7. The ratios of the bolometric luminosities and the Paschen line luminosities vary from $\sim 10^2$ to $\sim 10^4$. However, we do not find any trend of the ratio along with the bolometric luminosity even for very luminous objects ($L_{bol} > 10^{46}$ erg s^{-1}).

Moreover, we compare the bolometric corrections from the Paschen line luminosities with the λ_{Edd} values. In order to measure the λ_{Edd} values, BH masses are needed, and we adopted the BH masses from four previous papers (Peterson et al. 2004; Vestergaard & Peterson 2006; Landt et al. 2008; Kim et al. 2010). Among the 48 objects, 42 objects overlap with each other among these papers. For the overlapping objects, the BH masses determined from the reverberation mapping technique (Peterson et al. 2004) are used in preference to the BH masses from the single epoch techniques (Vestergaard & Peterson 2006; Landt et al. 2008; Kim et al. 2010; Jun et al. 2015). The BH masses listed in these papers are adopted

Table 6. Brackett line and bolometric luminosities.

Name	$L_{\mathrm{Br}\,\beta}$ (erg s^{-1})	$L_{\mathrm{Br}\,\alpha}$ (erg s^{-1})	L_{bol} (erg s^{-1})
3C 120	–	$10^{41.0\pm0.1}$	$10^{45.3\pm0.2}$
PG 0052+251	$10^{42.0\pm0.1}$	–	$10^{45.9\pm0.1}$
Mrk 79	$10^{40.9\pm0.1}$	–	$10^{44.3\pm0.0}$
Mrk 110	–	$10^{40.8\pm0.1}$	$10^{45.1\pm0.1}$
NGC 3783	–	$10^{40.6\pm0.1}$	$10^{44.2\pm0.1}$
NGC 4051	–	$10^{39.2\pm0.2}$	$10^{42.6\pm0.1}$
NGC 4151	$10^{39.9\pm0.1}$	$10^{40.1\pm0.0}$	$10^{44.0\pm0.1}$
3C 273	$10^{42.9\pm0.1}$	–	$10^{47.0\pm0.1}$
NGC 4593	–	$10^{40.2\pm0.1}$	$10^{43.7\pm0.0}$
PG 1411+442	$10^{41.9\pm0.1}$	$10^{42.1\pm0.1}$	$10^{45.4\pm0.0}$
NGC 7469	$10^{40.9\pm0.2}$	$10^{41.1\pm0.1}$	$10^{44.8\pm0.2}$

Note. Brackett line luminosities and bolometric luminosities. The Brackett line luminosity measurements come from Kim et al. (2015b), bolometric luminosity measurements come from Vasudevan & Fabian (2009).

after applying a recent virial coefficient of $\log f = 0.05$ (Woo et al. 2015), and the adopted BH masses are listed in Table 5. Using the bolometric luminosities and the adopted BH masses, we measure the λ_{Edd} values, and the measured $\log(\lambda_{\mathrm{Edd}})$ values vary from -3 to 0.5. We examined how the L_{bol} and Paschen line luminosity relations vary with λ_{Edd}, as shown in Figs 8 and 9. In Fig. 9, we show a difference between the observed L_{bol} values and the L_{bol} values from Paschen line luminosities along with λ_{Edd} and L_{bol}. We fit these quantities with a linear function, and the measured slopes are $\sim$0.39. However, the correlations between these quantities are not significant, which Pearson correlation coefficients are only $\sim$0.39. Note that the measured Kendall's and Spearman's rank correlation coefficients for the quantities are only $\sim$0.33 and $\sim$0.45, and their significances of the deviations from zero are $\sim$0.034 and $\sim$0.046, respectively. These results also support the result of Pearson correlation coefficient. Therefore, we conclude that the measured bolometric corrections using the Paschen line luminosities have no significant dependence on the bolometric luminosity nor λ_{Edd} over a wide range of bolometric luminosity (10^{41} erg s^{-1} $< L_{\mathrm{bol}} <$ 10^{48} erg s^{-1}) and λ_{Edd} ($-3 < \log(\lambda_{\mathrm{Edd}}) < 0.5$).

4.2 Accretion rates of red AGNs

As an application example of this study, we compare λ_{Edd} values of red AGNs and normal unobscured type 1 AGNs (hereafter, blue AGNs). In some simulation studies (e.g, Hopkins et al. 2005, 2008), intermediate stage galaxies between merger-driven star-forming phase and blue AGN phase are predicted to have more active and rapidly growing SMBHs than blue AGNs. However, the BH activities of these intermediate stage galaxies are concealed by dust in their host galaxies. Since red AGNs are suspected to be the intermediate stage galaxies, herein, we investigate whether red AGNs exhibit higher accretion rates than blue AGNs, as expected in the simulation studies.

In order to measure λ_{Edd}, the bolometric luminosities and BH masses are needed. Since red AGNs are heavily affected by the dust extinction (e.g. $E(B-V) > 0.1$; Glikman et al. 2007; Urrutia et al. 2009; Kim & Im 2018; Kim et al. 2018), we derive the bolometric luminosities of red AGNs by applying the Paschen-line-based bolometric correction, which are relatively immune from the dust extinction effects.

For estimating the λ_{Edd} values of red AGNs, we adopt red AGNs listed in two previous studies, Kim et al. (2015a) and Kim et al. (2018). Kim et al. (2015a) investigated 16 red AGNs at $z \sim 0.7$, and they were drawn from Glikman et al. (2007) and Urrutia et al. (2009). The red AGNs in Glikman et al. (2007) and Urrutia et al. (2009) were selected by using red colours through optical to NIR (e.g. $R-K>4$ and $J-K>1.7$ in Glikman et al. 2007; $r'-K>5$ and $J-K>1.3$ in Urrutia et al. 2009) with FIRST (Becker, White & Helfand 1995) radio detection, and their red colours arise from the dust obscuration ($E(B-V) > 0.1$; Glikman et al. 2007; Urrutia et al. 2009; Kim & Im 2018). Kim et al. (2015a) measured the dust extinction-corrected Pβ luminosities of the 16 red AGNs using the NIR spectra taken with SpeX on NASA IRTF. For correcting the dust extinction, they adopted the $E(B-V)$ values from previous studies (Glikman et al. 2007; Urrutia et al. 2009).

Kim et al. (2018) presented the result of optical and NIR spectroscopic observation of 16 red AGNs at $z \sim 0.3$ using ESI/Keck, GNIRS/Gemini, SpeX/IRTF, FIRE/Magellan, and IRCS/Subaru, and their Paschen line luminosities were provided. The 16 red AGNs were drawn from Marble et al. (2003), and these red AGNs were selected by a red colour in NIR ($J-K>2$; Cutri et al. 2001, 2002) among which some red AGNs cannot be inferred as dust obscured AGNs (i.e. $E(B-V) > 0.2$; Kim et al. 2018). It is suspected that the mildly obscured red AGN selection is due to the lack of optical through NIR colour selection (Kim et al. 2018). Among them, four red AGNs are dust obscured ($E(B-V) > 0.2$ in both methods based on the line-luminosity ratios and the continuum slope; see Section 4.3 of Kim et al. 2018 for more details), and we use only the four dust obscured objects as red AGNs in this study. The dust extinction-corrected Pβ and Pα luminosities of the four red AGNs were measured in Kim et al. (2018). We note that 2327 + 1624 is excluded, because its Pβ FWHM was not measured due to a broadly split Pβ line that make BH mass estimates very uncertain (e.g. Jun et al. 2017) and could be a sign of multiple interacting BHs rather than high BH mass (Kim et al. 2020).

In conclusion, we use 20 red AGNs that is composed of 4 low-z ($z \sim 0.3$) and 16 high-z ($z \sim 0.7$) sub-samples. For estimating their λ_{Edd} values, we adopt their Paschen line FWHM values and the dust extinction-corrected Paschen line luminosities.

For a comparison sample, we draw blue AGNs from Shen et al. (2011) of the Sloan Digital Sky Survey (SDSS) Seventh Data Release (DR7; Abazajian et al. 2009). In order to avoid the redshift bias effects, we choose the blue AGNs in the similar redshifts to the selected red AGNs: (i) $z \sim 0.3$ ($0.14 < z < 0.41$) and (ii) $z \sim 0.7$ ($0.56 < z < 0.84$) for low-z and high-z AGNs, respectively. Moreover, we choose the blue AGNs with the same Two Micron All-Sky Survey (2MASS; Skrutskie et al. 2006) K-band magnitudes of the selected red AGNs (12.9 mag $< K <$ 13.2 mag for low-z AGNs; 13.7 mag $< K <$ 15.2 mag for high-z AGNs) to avoid the sample selection bias effects.Through the above sample selection, finally, we select 35 and 579 blue AGNs at $z \sim 0.3$ and $z \sim 0.7$, respectively.

4.2.1 *BH masses*

For estimating BH masses of the red AGNs, we use the Paschen-line-based BH mass estimators (Kim et al. 2010, 2015a, 2018) to alleviate the dust extinction effects. Therefore, we use the Paschen-line-based BH mass estimators after applying the recent virial coefficient of $\log f = 0.05$ (Woo et al. 2015). The updated Paschen-line-based BH

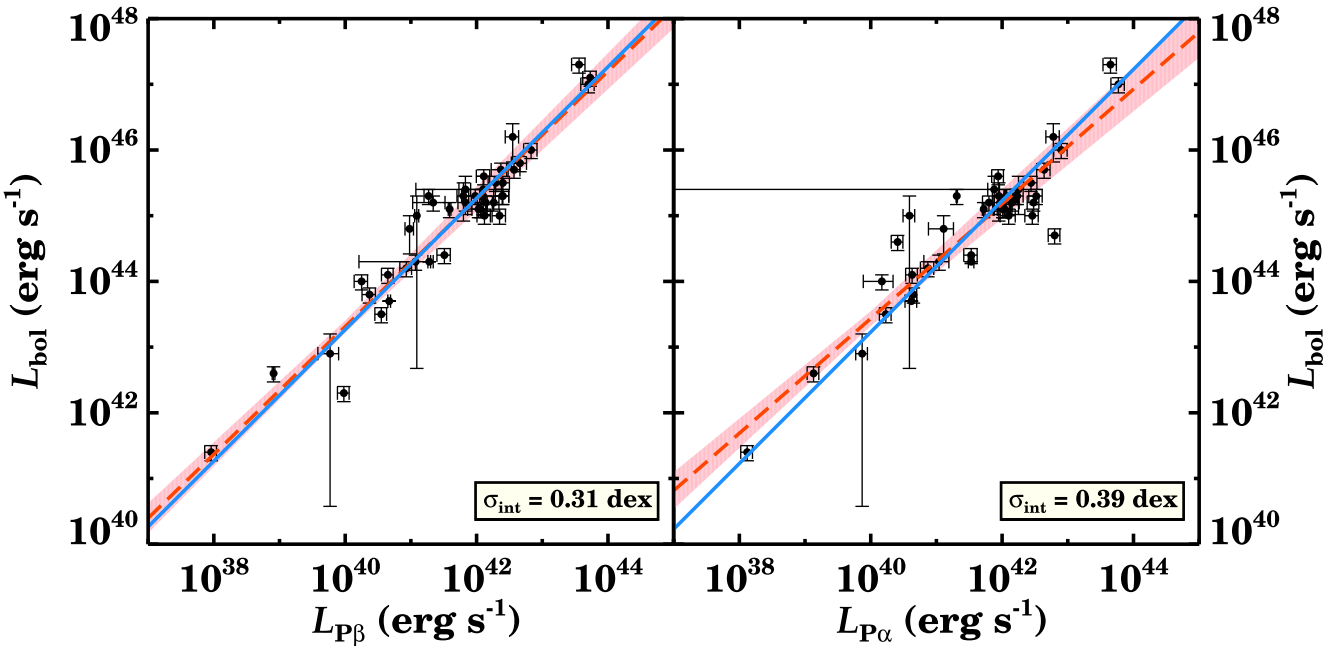

Figure 5. Relations between the Paschen line and bolometric luminosities. The blue solid lines and red dashed lines represent the best-fitting relations between the two quantities when the slope term B in equation (1) is set to 1 and free parameter, respectively. The pink bands indicate the 1 σ confidence ranges of the best-fitting relations when the slope term is set to the free parameter. In each panel, the intrinsic scatters of the points with respect to the blue solid line are marked.

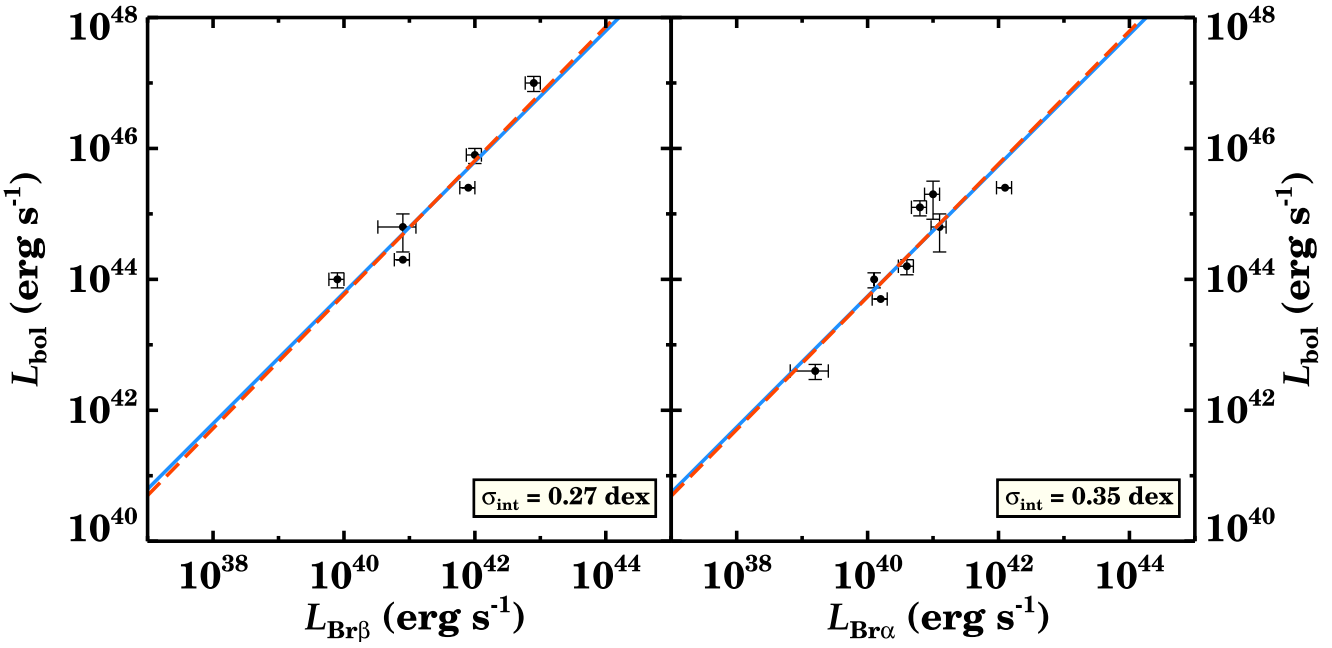

Figure 6. Relations between the Brackett line and bolometric luminosities. The blue solid lines and red dashed lines represent the best-fitting relations between the two quantities when the slope term B in equation (1) is set to 1 and free parameter, respectively. In each panel, the intrinsic scatters of the points with respect to the blue solid line are marked.

mass estimators with the new virial coefficient are

$$\frac{M_{\rm BH}}{M_\odot} = 10^{7.04\pm0.02}\left(\frac{L_{P\beta}}{10^{42}\,{\rm erg\,s^{-1}}}\right)^{0.48\pm0.03}\left(\frac{{\rm FWHM}_{P\beta}}{10^{3}\,{\rm km\,s^{-1}}}\right)^{2} \quad (2)$$

and

$$\frac{M_{\rm BH}}{M_\odot} = 10^{7.07\pm0.04}\left(\frac{L_{P\alpha}}{10^{42}\,{\rm erg\,s^{-1}}}\right)^{0.49\pm0.06}\left(\frac{{\rm FWHM}_{P\alpha}}{10^{3}\,{\rm km\,s^{-1}}}\right)^{2}. \quad (3)$$

In order to measure BH masses of the blue AGNs, we use the optical-based-BH mass estimator of McLure & Dunlop (2004).

Table 7. Bolometric luminosity estimators with Paschen and Brackett lines.

$L_{\rm bol}$–$L_{\rm Paschen}$ relationships	Intrinsic scatter
$\log\left(\frac{L_{\rm bol}}{10^{42}\,{\rm erg\,s^{-1}}}\right) = (1.31\pm0.09) + (0.97\pm0.05)\log\left(\frac{L_{\rm P\beta}}{10^{40}\,{\rm erg\,s^{-1}}}\right)$	0.31 dex
$\log\left(\frac{L_{\rm bol}}{10^{42}\,{\rm erg\,s^{-1}}}\right) = (1.27\pm0.05) + \log\left(\frac{L_{\rm P\beta}}{10^{40}\,{\rm erg\,s^{-1}}}\right)$	0.31 dex
$\log\left(\frac{L_{\rm bol}}{10^{42}\,{\rm erg\,s^{-1}}}\right) = (1.43\pm0.11) + (0.87\pm0.06)\log\left(\frac{L_{\rm P\alpha}}{10^{40}\,{\rm erg\,s^{-1}}}\right)$	0.37 dex
$\log\left(\frac{L_{\rm bol}}{10^{42}\,{\rm erg\,s^{-1}}}\right) = (1.23\pm0.07) + \log\left(\frac{L_{\rm P\alpha}}{10^{40}\,{\rm erg\,s^{-1}}}\right)$	0.39 dex
$\log\left(\frac{L_{\rm bol}}{10^{42}\,{\rm erg\,s^{-1}}}\right) = (1.77\pm0.25) + (1.02\pm0.15)\log\left(\frac{L_{\rm Br\beta}}{10^{40}\,{\rm erg\,s^{-1}}}\right)$	0.31 dex
$\log\left(\frac{L_{\rm bol}}{10^{42}\,{\rm erg\,s^{-1}}}\right) = (1.80\pm0.13) + \log\left(\frac{L_{\rm Br\beta}}{10^{40}\,{\rm erg\,s^{-1}}}\right)$	0.27 dex
$\log\left(\frac{L_{\rm bol}}{10^{42}\,{\rm erg\,s^{-1}}}\right) = (1.73\pm0.19) + (1.01\pm0.18)\log\left(\frac{L_{\rm Br\alpha}}{10^{40}\,{\rm erg\,s^{-1}}}\right)$	0.38 dex
$\log\left(\frac{L_{\rm bol}}{10^{42}\,{\rm erg\,s^{-1}}}\right) = (1.74\pm0.14) + \log\left(\frac{L_{\rm Br\alpha}}{10^{40}\,{\rm erg\,s^{-1}}}\right)$	0.35 dex

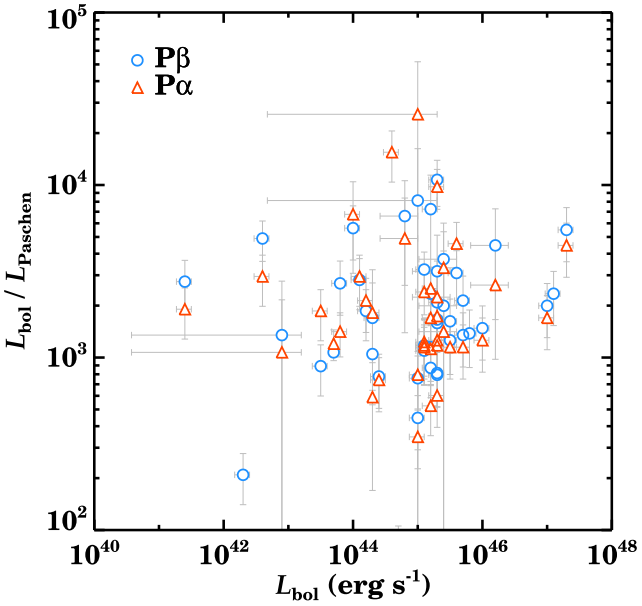

Figure 7. Luminosity ratios of $L_{\rm bol}$ to $L_{\rm Paschen}$ as a function of the bolometric luminosity. The blue circles and red triangles are for the P β and P α lines, respectively.

The optical-based-BH mass estimator consist of $\lambda L_{5100\text{Å}}$ (hereafter, L5100) and FWHM of the H β line (FWHM$_{\rm H\beta}$), and these parameters of the blue AGNs are taken from Shen et al. (2011). The optical-based-BH mass estimator is modified by applying the new virial coefficient, which is

$$\frac{M_{\rm BH}}{M_\odot} = 5.27\left(\frac{\rm L5100}{10^{44}\,{\rm erg\,s^{-1}}}\right)^{0.61}\left(\frac{\rm FWHM_{H\beta}}{\rm km\,s^{-1}}\right)^2. \quad (4)$$

4.2.2 *Bolometric luminosities*

To obtain the bolometric luminosities of red AGNs, we use the Paschen-line-based bolometric luminosity estimators derived in Section 3. However, the bolometric luminosities of blue AGNs are measured from the L5100 values with a bolometric correction factor of 9.26 (Shen et al. 2011).

4.2.3 *Eddington ratios*

We compare $\lambda_{\rm Edd}$ values of the red and blue AGNs. First, for the low-z sub-sample, 4 red AGNs and 35 blue AGNs are used for the comparison. The mean $\log(\lambda_{\rm Edd})$ values of the red and blue AGNs are -0.64 ± 0.26 and -0.63 ± 0.07, respectively, and this comparison is presented in Fig. 10. In order to quantify the difference between the $\log(\lambda_{\rm Edd})$ distributions of these two AGN populations, we perform the Kolmogorov–Smirnov test (K–S test) using the KSTWO code based on the IDL. The maximum deviation between the two cumulative distributions, D, is 0.19, and the probability of the result given the null hypothesis, p, is 0.99. These results show that the $\log(\lambda_{\rm Edd})$ values of red AGNs are similar with those of blue AGNs.

Secondly, we compare the $\lambda_{\rm Edd}$ values of red and blue AGNs at $z\sim0.7$. For the high-z sub-sample, 16 red AGNs and 579 blue AGNs are used for the comparison. The comparison is presented in Figs 10 and 11, and the average $\log(\lambda_{\rm Edd})$ of the red AGNs, -0.19 ± 0.09, is significantly higher than that of the blue AGNs, -0.65 ± 0.02. Moreover, for the K–S statistics, the $\lambda_{\rm Edd}$ distributions of the two AGNs have the D of 0.57 and the p of 3.8×10^{-5}. These results show that the $\lambda_{\rm Edd}$ values of red AGNs are significantly higher than those of blue AGNs at $z\sim0.7$.

Moreover, to figure out the higher $\lambda_{\rm Edd}$ values of the blue AGNs does not arise from difference in the $\lambda_{\rm Edd}$ estimators, we newly measure the $\lambda_{\rm Edd}$ values of the blue AGNs using the Paschen line, as the $\lambda_{\rm Edd}$ values of the red AGNs are measured. For the 579 blue AGNs at $z\sim0.7$, we convert their H β FWHMs and luminosities adopted from Shen et al. (2011) to the P β FWHMs and luminosities using the relationships of table 2 in Kim et al. (2010). After that, we obtain the P β-line-based bolometric luminosities using the converted P β line luminosities with the relation in equation (1) when the slope term B is set to free parameter. In addition, the P β-line-based BH masses are measured using the converted P β FWHMs and luminosities with the equation (2). Although the newly measured P β-line-based $\lambda_{\rm Edd}$ values (-0.56 ± 0.02) of blue AGNs are somewhat higher than the $\lambda_{\rm Edd}$ values from optical estimators, the $\lambda_{\rm Edd}$ values of red AGNs are still significantly higher than those of blue AGNs. Moreover, the D and p values from the K–S test between the two distributions are 0.46 and 0.0017, respectively. This result is consistent with the above result.

Since $\lambda_{\rm Edd}$ values can vary with bolometric luminosities (e.g. Lusso et al. 2012; Suh et al. 2015), we compare the $\lambda_{\rm Edd}$ values after dividing the high-z sub-sample into two sub-samples composed

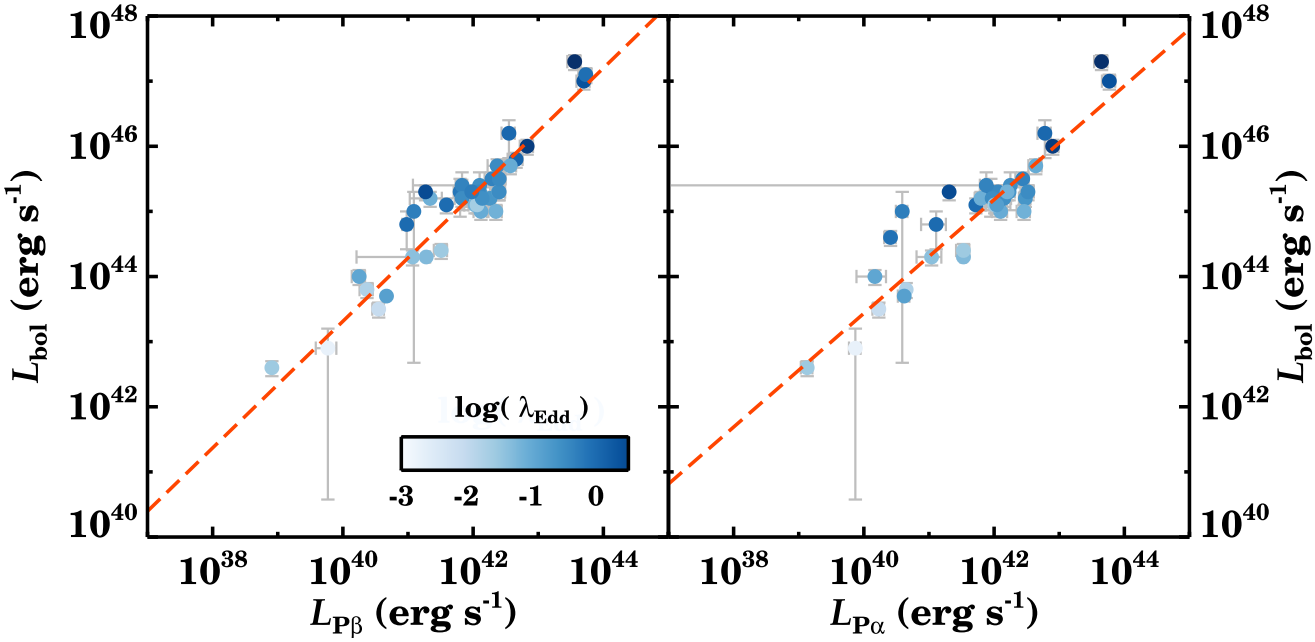

Figure 8. Comparisons between L_{bol} and $L_{Paschen}$ values, and the colours in the circles indicate their λ_{Edd} values as shown in the legend.

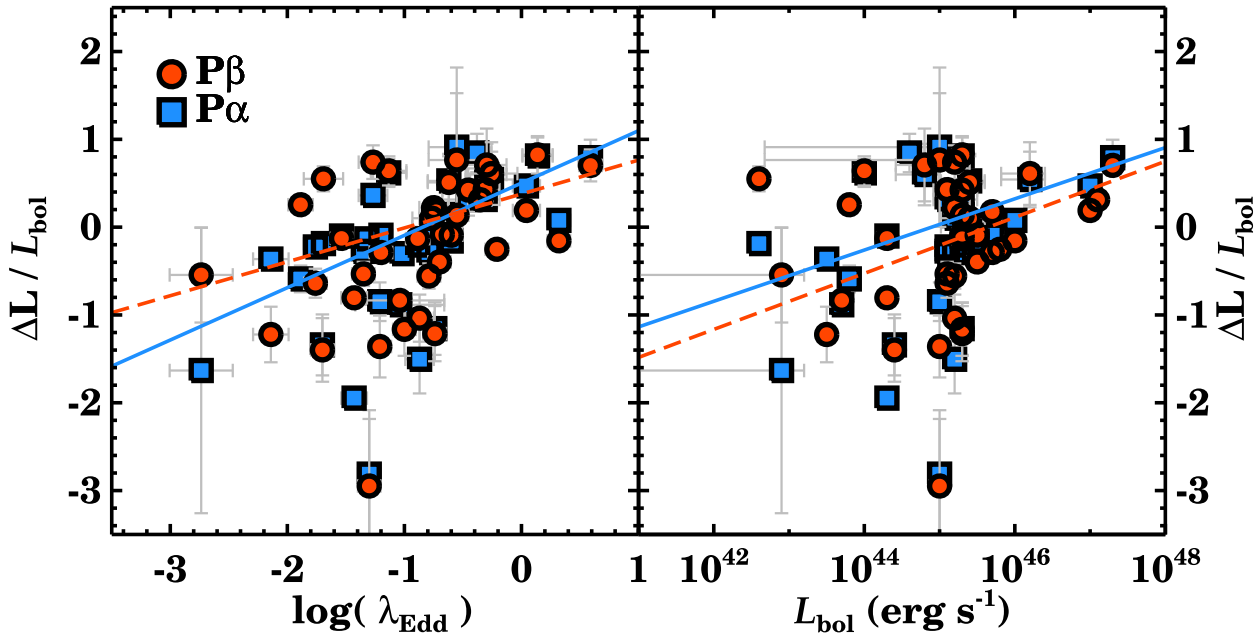

Figure 9. (Left-hand panel) Luminosity ratios of ΔL to L_{bol} as a function of λ_{Edd}, where ΔL is a difference between the observed L_{bol} values and the L_{bol} values from Paschen line luminosities with equation (1) when the slope term B in equation (1) is set to free parameter. The red dashed and the blue solid lines represent the best fit with a linear function for the P β and P α lines, respectively. (Right-hand panel) Luminosity ratios of ΔL to L_{bol} as a function of L_{bol}. The meanings of the lines are identical.

of (i) low ($46.1 < \log(L_{bol} / \mathrm{erg\,s^{-1}}) < 46.3$) and (ii) high bolometric luminosity sub-sample ($46.5 < \log(L_{bol} / \mathrm{erg\,s^{-1}}) < 47.1$). These comparisons are presented in Fig. 11. For the low bolometric luminosity sub-sample, 8 red AGNs and 199 blue AGNs are used for the comparison. The mean $\log(\lambda_{Edd})$ values of the red and blue AGNs are -0.38 ± 0.10 and -0.68 ± 0.03, respectively. For the high bolometric luminosity sub-sample, another half, 8 red AGNs and 147 blue AGNs are chosen, and their mean $\log(\lambda_{Edd})$ values are -0.00 ± 0.11 and -0.50 ± 0.03, respectively. These results confirm that red AGNs at $z \sim 0.7$ have significantly higher λ_{Edd} values than blue AGNs regardless of bolometric luminosities.

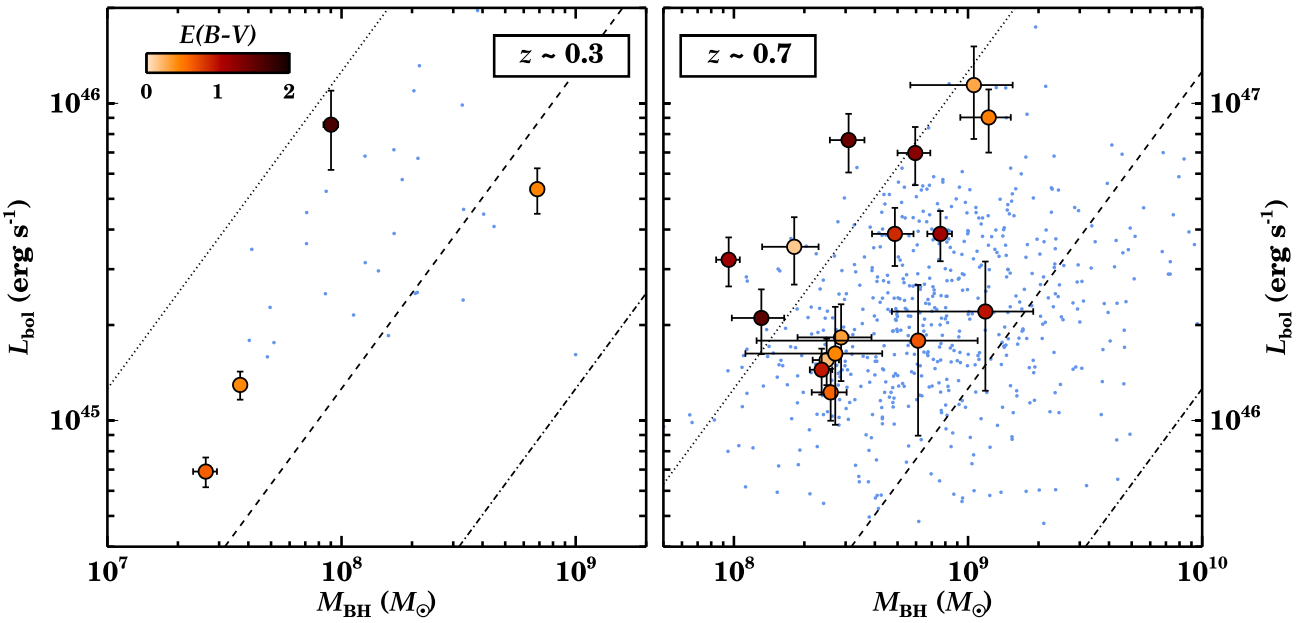

Figure 10. (Left-hand panel) Bolometric luminosities versus BH masses of red and blue AGNs at $z \sim 0.3$. The red AGNs are marked with open circles, and the colours in the circles mean their $E(B-V)$ values. The blue AGNs are shown with blue dots. The dot-dashed, dashed, and dotted lines indicate λ_{Edd} of 0.01, 0.1, and 1.0, respectively. (Right-hand panel) Bolometric luminosities versus BH masses of red and blue AGNs at $z \sim 0.7$. The meanings of red circles, blue dots, and three lines are identical to those of the left-hand panel.

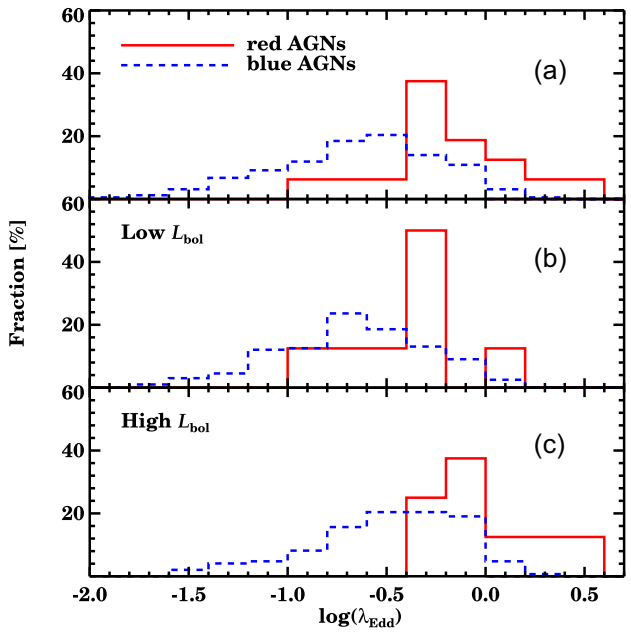

Figure 11. (a) The λ_{Edd} distributions of red and blue AGNs at $z \sim 0.7$. The red solid and blue dashed histograms mean the λ_{Edd} distributions of red and blue AGNs, respectively. (b) The λ_{Edd} distributions for the low bolometric luminosity sample ($46.09 < \log(L_{bol} / \mathrm{erg\,s^{-1}}) < 46.34$). (c) The λ_{Edd} distributions for the high bolometric luminosity sample ($46.51 < \log(L_{bol} / \mathrm{erg\,s^{-1}}) < 47.06$).

The result that red AGNs have higher $\log(\lambda_{Edd})$ values than blue AGNs at $z \sim 0.7$ support the scenario that red AGNs are the intermediate stage galaxies between merger-driven star-forming galaxies and visible blue AGNs. These result is consistent with previous studies (Urrutia et al. 2012; Kim et al. 2015a; Kim & Im 2018). However, the $\log(\lambda_{Edd})$ values of red AGNs are not significantly higher than those of blue AGNs at $z \sim 0.3$. This discrepant result at $z \sim 0.3$ could arise from (i) the insufficient number of red AGNs in the comparison, or (ii) red AGNs at $z \sim 0.3$ originate through a different formation mechanism, and this could be a reason of the inconsistent observational results of red AGNs to date (e.g. Puchnarewicz & Mason 1998; Whiting, Webster & Francis 2001; Wilkes et al. 2002; Rose et al. 2013). In order to check the proposition, more extensive investigations for red AGNs at $z \sim 0.3$ are needed.

5 CONCLUSIONS

In order to establish bolometric luminosity estimators relatively immune from dust extinction effects, we examined the relationships between bolometric luminosities and IR hydrogen emission line luminosities, such as Paschen and Brackett lines, for 48 unobscured type 1 AGNs. We found tight correlations between bolometric luminosities and IR line luminosities, which can be applied to measure the bolometric luminosities of dust obscured AGNs.

We applied the Paschen-line-based bolometric luminosity estimator to red AGNs that have been suspected as dust obscured young AGNs. Using the newly measured bolometric luminosities of red AGNs, the λ_{Edd} ratios were higher than unobscured type 1 AGNs, as expected in previous simulation studies, and in agreement with previous observational studies.

The derived IR line bolometric estimators can be extensively used through future NIR and MIR space missions, such as *SPHEREx* and *James Webb Space Telescope*. These space missions are sensitive enough to detect IR hydrogen emission lines of dust obscured AGNs at relatively high redshifts. Such measurements will help us understand the cosmic evolution of dust obscured AGNs by overcoming the dust extinction effects.

ACKNOWLEDGEMENTS

We are grateful to the anonymous referee for useful comments which improved the manuscript. This work was supported by a 2-Year Research Grant of Pusan National University.

DATA AVAILABILITY

The data underlying this article are available in the article and in its online supplementary material.

REFERENCES

Abazajian K. N. et al., 2009, ApJS, 182, 543
Antonucci R., 1993, ARA&A, 31, 473
Baumgartner W. H. et al., 2013, ApJS, 207, 19
Becker R. H., White R. L., Helfand D. J., 1995, ApJ, 450, 559
Brightman M. et al., 2017, ApJ, 844, 10
Cutri R. M., Nelson B. O., Kirkpatrick J. D., Huchra J. P., Smith P. S., 2001, in Roger C., Andrew A., Gordon B., eds, ASP Conf. Ser. Vol. 232, The New Era of Wide Field Astronomy. Astron. Soc. Pac., San Francisco, p. 78
Cutri R. M., Nelson B. O., Francis P. J., Smith P. S., 2002, in Green R. F., Khachikian E. Ye, Sanders D. B., eds, IAU Colloq. 184: AGN Surveys, ASP Conf. Proc., Vol. 284, Astron. Soc. Pac., San Francisco,p. 127
Di Matteo T., Springel V., Hernquist L., 2005, Nature, 433, 604
Elvis M. et al., 1994, ApJS, 95, 1
Georgakakis A. et al., 2009, MNRAS, 394, 533
Glikman E., Helfand D. J., White R. L., 2006, ApJ, 640, 579
Glikman E. et al., 2007, ApJ, 667, 673
Glikman E. et al., 2015, ApJ, 806, 218xs
Hopkins P. F. et al., 2005, ApJ, 630, 705
Hopkins P. F., Hernquist L., Cox T. J., Kereš D., 2008, ApJS, 175, 356
Im M., Griffiths R. E., Ratnatunga K. U., 1997, ApJ, 475, 457
Jun H. D. et al., 2015, ApJ, 806, 109
Jun H. D. et al., 2017, ApJ, 838, 41
Kaspi S. et al., 2000, ApJ, 533, 631
Kim D., Im M., 2018, A&A, 610, A31
Kim D., Im M., Kim M., 2010, ApJ, 724, 386
Kim D. et al., 2015a, ApJ, 812, 66
Kim D. et al., 2015b, ApJS, 216, 17
Kim D. et al., 2018, ApJS, 238, 37
Kim D. et al., 2020, ApJ, 894, 126
Krawczyk C. M. et al., 2013, ApJS, 206, 4
Lamperti I. et al., 2017, MNRAS, 467, 540
Landt H. et al., 2008, ApJS, 174, 282
Lusso E. et al., 2012, MNRAS, 425, 623
Marble A. R. et al., 2003, ApJ, 590, 707
Marconi A. et al., 2004, MNRAS, 351, 169
Markwardt C. B., 2009, in Bohlender D. A., Daniel D., Patrick D., eds, ASP Conf. Ser. Vol. 411, Astronomical Data Analysis Software and Systems XVIII. Astron. Soc. Pac., San Francisco, p. 251
McLure R. J., Dunlop J. S., 2004, MNRAS, 352, 1390
Peterson B. M. et al., 2004, ApJ, 613, 682
Planck Collaboration VIII 2011, A&A, 536, A16
Planck Collaboration XIII 2016, A&A, 594, A13
Puchnarewicz E. M., Mason K. O., 1998, MNRAS, 293, 243
Reeves J. N. et al., 2009, ApJ, 701, 493
Richards G. T. et al., 2006, ApJS, 166, 470
Riffel R., Rodríguez-Ardila A., Pastoriza M. G., 2006, A&A, 457, 61
Rose M., Tadhunter C. N., Holt J., Rodríguez Zaurín J., 2013, MNRAS, 432, 2150
Ruiz A. et al., 2010, A&A, 515, A99
Runnoe J. C., Brotherton M. S., Shang Z., 2012, MNRAS, 422, 478
Sanders D. B. et al., 1988, ApJ, 325, 74
Shang Z. et al., 2011, ApJS, 196, 2
Shen Y. et al., 2011, ApJS, 194, 45
Skrutskie M. F. et al., 2006, AJ, 131, 1163
Sobolewska M. A., Siemiginowska A., Życki P. T., 2004, ApJ, 608, 80
Sobolewska M. A., Siemiginowska A., Życki P. T., 2004, ApJ, 617, 102
Steffen A. T. et al., 2006, AJ, 131, 2826
Suh H., Hasinger G., Steinhardt C., Silverman J. D., Schramm M., 2015, ApJ, 815, 129
Urrutia T., Lacy M., Becker R. H., 2008, ApJ, 674, 80
Urrutia T. et al., 2009, ApJ, 698, 1095
Urrutia T. et al., 2012, ApJ, 757, 125
Vasudevan R. V., Fabian A. C., 2007, MNRAS, 381, 1235
Vasudevan R. V., Fabian A. C., 2009, MNRAS, 392, 1124
Vasudevan R. V. et al., 2009, MNRAS, 399, 1553
Veilleux S., Kim D.-C., Sanders D. B., 2002, ApJS, 143, 315
Vestergaard M., Peterson B. M., 2006, ApJ, 641, 689.
Whiting M. T., Webster R. L., Francis P. J., 2001, MNRAS, 323, 718
Wilkes B. J. et al., 2002, ApJL, 564, L65
Williams M. J., Bureau M., Cappellari M., 2010, MNRAS, 409, 1330
Woo J.-H., Yoon Y., Park S., Park D., Kim S. C., 2015, ApJ, 801, 38

This paper has been typeset from a TEX/LATEX file prepared by the author.